TU Delft

Delft University of Technology

Document Version
Final published version

Licence
CC BY

Citation (APA)
Maldonado de León, H., Straathof, A., & Haringa, C. (2025). Dynamic compartment models: Towards a rapid modeling approach for fed-batch fermentations. *Chemical Engineering Science*, *308*, Article 121396. https://doi.org/10.1016/j.ces.2025.121396

Important note
To cite this publication, please use the final published version (if applicable).
Please check the document version above.

Copyright
In case the licence states “Dutch Copyright Act (Article 25fa)”, this publication was made available Green Open Access via the TU Delft Institutional Repository pursuant to Dutch Copyright Act (Article 25fa, the Taverne amendment). This provision does not affect copyright ownership.
Unless copyright is transferred by contract or statute, it remains with the copyright holder.

Sharing and reuse
Other than for strictly personal use, it is not permitted to download, forward or distribute the text or part of it, without the consent of the author(s) and/or copyright holder(s), unless the work is under an open content license such as Creative Commons.

Takedown policy
Please contact us and provide details if you believe this document breaches copyrights.
We will remove access to the work immediately and investigate your claim.

This work is downloaded from Delft University of Technology.

Chemical Engineering Science 308 (2025) 121396

Contents lists available at ScienceDirect

Chemical Engineering Science

journal homepage: www.elsevier.com/locate/ces

Dynamic compartment models: Towards a rapid modeling approach for fed-batch fermentations

Héctor Maldonado de León *, Adrie Straathof, Cees Haringa

Department of Biotechnology, Delft University of Technology, Van der Maasweg 9, Delft, 2629 HZ, The Netherlands

ARTICLE INFO

Dataset link: https://doi.org/10.4121/0a08d2ec-8959-403f-afea-2b085dc9f3a6

Keywords:
Surrogate model
CFD
Bioreactor modeling
Dynamic compartment model
Fed-batch simulation

ABSTRACT

Anticipating the occurrence and effects of mass transport limitations during fermentation scale-up is essential for commercialization, as heterogeneities might affect microorganisms. Tools like Computational Fluid Dynamics (CFD) aid this analysis but are computationally intensive, limiting design space exploration and consequently, fermentation optimization. Compartment models (CMs) based on CFD simulations offer an affordable alternative but require CFD recalibration with changing geometries or operating conditions, restricting their usage in optimization.

In this work, we introduce a hybrid machine-learning-aided compartment model (ML-CM) that accounts for flow pattern dynamics upon changes in both volume and stirring speed in a stirred tank bioreactor. The ML-aided dynamic compartment model (dyn-CM) enabled the spatiotemporal study of a process in 1/500th of the fermentation simulation time, maintaining reasonable accuracy. This method facilitates fed-batch fermentation modeling, process optimization, and scale-up effect analysis with modest computational resources, supporting reactor design and operational improvements within a defined operating space.

1. Introduction

Scaling up fermentation processes is a critical step in bioprocess development; as scale-up is challenging and expensive, it is sometimes called 'the (bioprocess) valley of death' (Kampers et al., 2022). Scaling effects are regarded as responsible for performance losses and their mitigation has proved to be expensive and time-consuming (Crater and Lievense, 2018; Delvigne et al., 2017; Herwig et al., 2021; Kampers et al., 2022; Noorman, 2011). One of the challenges upon scale-up is that the concentration gradients experienced by cells change with scale due to transport limitations, which may induce changes in the cellular response, and therefore affect process performance (Bylund et al., 1998; Haringa et al., 2018; Xu et al., 1999). To reduce the risk of unanticipated performance loss, scale-down studies, where cells are subjected to variations in their environment may be conducted (Lara et al., 2006; Neubauer and Junne, 2010). However, such studies typically only provide qualitative insights into the potential of productivity losses. This led to a rising interest in model-based approaches, where detailed hydrodynamic models and cell kinetic models are coupled to make scale-up performance predictions for specific reactor systems. Typically, this has been addressed using a validated framework based on Computational Fluid Dynamics (CFD) (Delvigne et al., 2017; Herwig et al., 2021; Lapin Alexei and Reuss, 2004, 2006). The drawback of these models is their high computational demand, which means that only one or a few operating conditions may be assessed, making the methods unsuitable for (iterative) process optimization. Additionally, the conditions inside the reactor are assumed to be stationary (Haringa et al., 2018; Puiman et al., 2022; Siebler et al., 2019). In reality, fermentations are typically dynamic fed-batch operations, in which liquid volume and operating conditions change in time. Current state-of-the-art CFD simulations cannot feasibly account for this due to computational expense and time demand. Hence, to consider the impact of heterogeneous conditions inside the bioreactor on process performance over the full process duration, and to optimize (dynamic) process conditions, computationally cheaper methods, that still feature adequate spatial resolution, are required. Compartment-based models (CMs) are an example of such computationally cheaper methods (Cui et al., 1996; Vrábel et al., 2000) where the bioreactor is approximated as a network of ideally mixed sub-volumes or 'compartments' (Delafosse, 2014; Nadal-Rey et al., 2021a).

While a high spatial resolution (1×10^6 mesh elements) is required to accurately solve flowfields from first principles (Haringa et al., 2018), a lower spatial resolution (1×10^3 mesh elements) typically suffices to

* Corresponding author.
E-mail address: H.A.MaldonadodeLeon@tudelft.nl (H. Maldonado de León).

https://doi.org/10.1016/j.ces.2025.121396
Received 11 December 2024; Received in revised form 3 February 2025; Accepted 17 February 2025
Available online 20 February 2025
0009-2509/© 2025 The Authors. Published by Elsevier Ltd. This is an open access article under the CC BY license (http://creativecommons.org/licenses/by/4.0/).

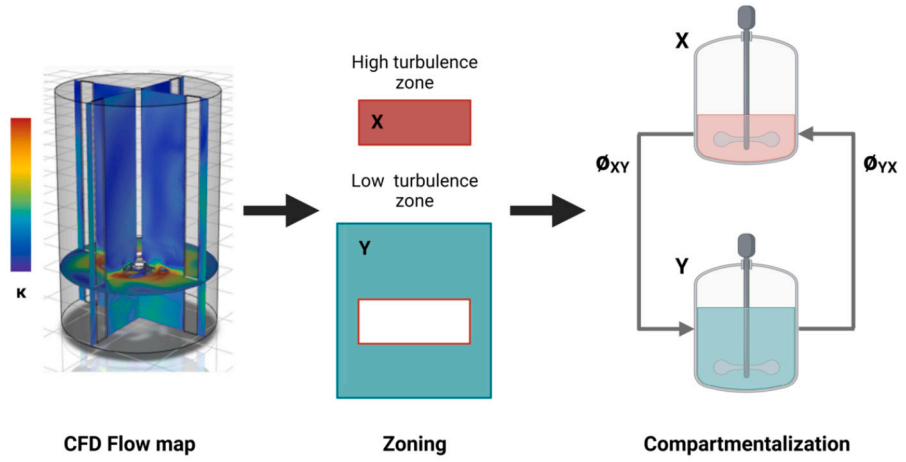


Fig. 1. Concept of a compartment model (CM) for two zones defined based on the turbulent kinetic energy for a stirred tank reactor.

capture phenomena relevant to process performance, such as mixing and subsequent gradients in substrate concentration, once the flowfield is known (Haringa et al., 2022). A simple depiction of these compartments is shown in Fig. 1. Each compartment corresponds to a local zone of the fluid and the interaction between the compartments is used to describe the transport mechanisms within the reactor. Prior studies utilizing CM have shown good performance in predicting mixing, gradient occurrence, and productivity when compared with CFD models, at a fraction of the computation time for CFD (De Carfort et al., 2024; Nadal-Rey et al., 2021a; Tajsoleiman et al., 2019). This is due to the decoupling of phenomena in compartment models making their runtimes significantly shorter than those of a fully-coupled CFD model (Jourdan et al., 2019).

The main objective of spatially-resolved bioreactor models is to study heterogeneity in nutrient availability, which follows from an interplay between localized feeding, biokinetics (i.e., consumption rate), hydrodynamics (i.e., mixing), and reactor design and type (Nadal-Rey et al., 2021b). Hence, it is key the CM replicates large-scale mixing with sufficient accuracy that depends on its parameterization, e.g. the number of compartments, their volumes, connections among them, and the exchange flow formulation (Delafosse, 2014; Tajsoleiman et al., 2019). The first generation of compartment models was manually configured (Cui et al., 1996; Jourdan et al., 2019; Vrábel et al., 2000), relying strongly on the user's expertise. Later approaches used detailed CFD simulations to configure the compartments via a 'zoning' algorithm (Delafosse, 2014; Nadal-Rey et al., 2021a; Tajsoleiman et al., 2019). In these approaches, a compartment map of the reactor is created based on hydrodynamic parameters like axial, and radial velocities (Nadal-Rey et al., 2021a; Tajsoleiman et al., 2019) and the turbulent energy dissipation rate (Bai et al., 2023), among others.

Still, despite the relevance of fed-batch operation most compartment models currently consider steady-state operation. One underlying reason is that, upon changing hydrodynamic conditions, new CFD simulations are required to calibrate the CM. However, once the CM has been constructed, it can be used to quickly assess various scenarios, such as different feed locations (Losoi et al., 2022), feed rates, or cell kinetics (Haringa et al., 2022), provided that the hydrodynamics do not substantially change. With this, significant computational reductions can be achieved when assessing or optimizing for a given hydrodynamic condition.

Prior studies have suggested several strategies for recalibrating the exchange flows across compartments ($\phi_{i,j}$). For steady-state simulations, linear correlations are based on changes in dimensionless numbers (Bai et al., 2023), stirring speed, or power input as proposed by Tajsoleiman et al. (2019). However, this methodology cannot deal with changes in the operating volume, which does not just change the magnitude of the flowrates, but also the flow pattern. Hence, we seek to develop a more general methodology that can deal with such dynamics. For this, a step-wise interpolation was presented to handle discrete changes in volume for a fed-batch fermentation by recalibrating the compartment model at given time points with new CFD data (Nadal-Rey et al., 2021a).

However, the requirement to run several CFD simulations to recalibrate the CM upon volume changes adds considerable computational cost, negating an advantage of compartment modeling. This is especially true in cases of process optimization where many (dynamic) conditions are to be evaluated, or when including process control in the simulation, in which case the process dynamics are not known upfront and need to be resolved during runtime (Oliveira et al., 2024). To cope with such situations, a methodology flexible enough to adapt the compartment parameterization (i.e. volumes and exchange flowrates) for certain operating conditions (e.g. volume, stirring speed), without requiring a CFD re-run, is desired.

Hence, we present a method in which CFD data are used to train a machine learning (ML) model, that will provide a compartment parameterization as output, given the filling volume (V_L) and stirring speed (N_s) as inputs. We will test our framework on the exchange flows given a fixed grid for a single-phase stirred tank at different filling volumes equipped with a Rushton impeller (max. 133 m^3). Our work aims to show that coupling a CFD-CM with an ML algorithm allows rapid and sufficiently accurate representation of flow features within the vessel, enabling design space exploration and full simulation of a fed-batch fermentation.

2. Materials and methods

In this section, we present the models and methods used to deploy the modeling workflow. We describe the aim of the approach including the reactor and process we modeled, the setup of the CFD models used to obtain the training data, the settings of the respective compartment-based models, and the interpolating module (i.e., the neural-network-based module).

2.1. Proposed workflow

A library of hydrodynamic data (i.e., frozen flow maps) was collected for different operating conditions using a conventional CFD approach, which was considered the ground truth for subsequent analyses. Further details of the operating conditions can be consulted in Appendix A.4. A set of CM realizations was generated from the CFD simulations to train the neural network used to create compartment-based parameterizations at any given working volume. These parameterizations allowed for the analysis of the evolution of substrate stratification during the fermentation. Fig. 2 depicts the workflow used in this work.

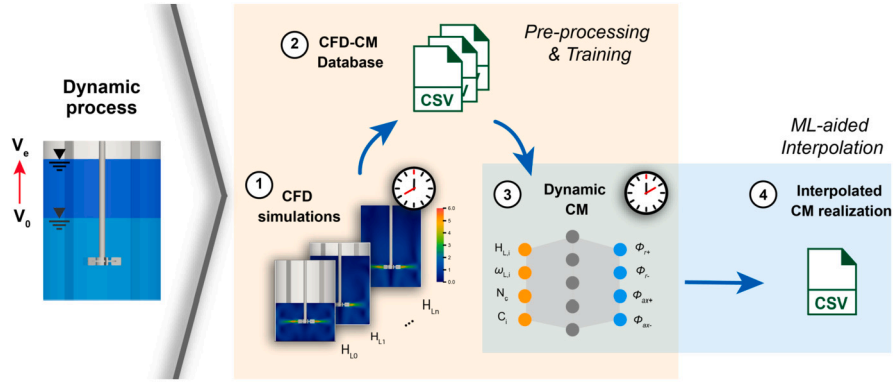


Fig. 2. Workflow for analyzing scale-up effects under dynamic conditions (i.e., variation of liquid heights - H_L) using compartment models (CMs) and a neural network as an inferring module for new CM realizations.

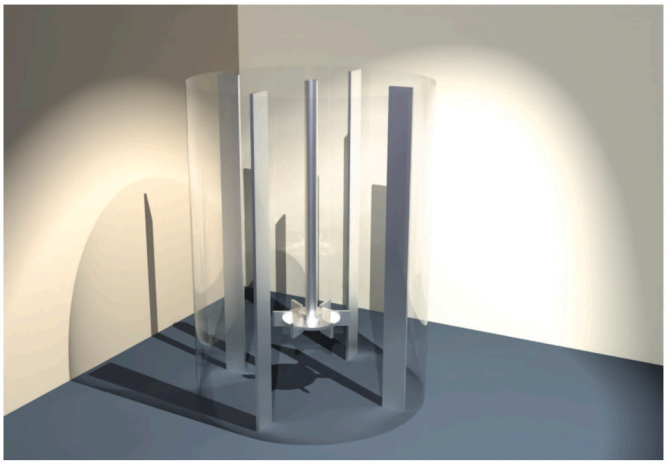


Fig. 3. Artistic representation of the 133 m^3 reactor evaluated.

2.2. The reactor model and operating conditions

A 133 m^3 stirred vessel ($T = 5$ m) with a single Rushton turbine (RT) and 4 baffles was considered. The aspect ratios are: for the impeller ($D = T/3$), baffles ($B = T/10$), and clearance from the bottom of the vessel to the impeller ($C = T/3$) (Couper et al., 2012). A sketch of the reactor is shown in Fig. 3 and further details about the dimensions of the geometry can be found in Appendix A.1 (see Fig. A.13). The properties of the media were assumed to be the ones of water at 20 °C (i.e., $\rho = 998.2\,kg\,m^{-3}$, $\mu = 1.003$ mPa s).

2.3. CFD setup

Single-phase simulations were conducted using Ansys FLUENT™ 2023R1 with GPU acceleration to obtain flow maps for different filling volumes of the stirred tank ranging from 63.5 to 133 m^3 and different stirring speeds ranging from 0.25 up to 1.46 s^{-1}. Within this operating range, the specific power input (ϵ) varies from 3.95×10^{-5} to $1.52\,W\,kg^{-1}$.

The multiple reference frame (MRF) approach and the standard $k-\varepsilon$ turbulence model were used to simulate the movement of the impeller and turbulent flow conditions, respectively. The mesh used for the spatial discretization of the system consisted of around 2 million cells. The walls were assumed to have a no-slip condition, and the top wall that simulated the liquid's free surface had a no-shear condition (i.e. 0 Pa). The simulations were considered to have converged once the residuals were lower than $O(10^{-4})$ and a coefficient of variation (CV) for the impeller's torque of less than 1 % was obtained.

The software was run in a workstation equipped with 16 AMD Ryzen ThreadripperPRO™ 5955WX CPUs, 64 GB RAM, and an Nvidia GeForce RTX 3090 graphics card. Mixing time determination for these simulations was conducted using frozen flow fields. Details about the settings of the methods and controls implemented in the simulations can be found in Appendix A.3.

2.4. The compartment model (CM)

Fixed compartment layouts, with equal-volume compartments, assuming axisymmetry were defined for this study and were labeled by the number of divisions in the axial (N_{ax}) and radial ($N_r = 5$) directions as follows A[N_{ax}]R[N_r]. For the axial direction, a compartment height (d_h) of 15 cm was determined as the suitable parameter after evaluating different layouts (see Appendix B.1). This layout showed the best agreement of the studied layouts with the frozen flow field calculated from CFD. We used planar data (2D) from the CFD simulations to calibrate the compartment models, following (Tajsoleiman et al., 2019) to be data-efficient, but our approach can equally be applied to CM on 3D data as in (Haringa et al., 2022). From the CFD models solved in FLUENT™, the values for the velocity components, coordinates, and turbulence kinetic energy were extracted from the nodes of an XY-plane rotated 45° along the Z-axis (see Fig. 4). These data were stored as `.csv` files, which makes the routine CFD-platform agnostic.

From these files, the intercompartment flow rates ($\phi_{(i,j)}$) were calculated using a Python script according to the approach outlined in (Delafosse, 2014; Haringa et al., 2022; Tajsoleiman et al., 2019). These flow rates are assumed to result from the contribution of a convective and turbulent term to account for the major mechanisms responsible for momentum transfer in such a closed system (Delafosse, 2014):

$$\phi_{(i,j)} = \phi_{c(i,j)} + \phi_{t(i,j)} \tag{1}$$

For the boundary sampling distance (d_b) a value of 2 cm at both sides from each intercompartmental boundary was set, and the average velocity across faces was weighed by the relative distance of the sampled points to the boundary. When less than 2 extracted data points were available within the d_b distance, an interpolation routine was employed to estimate the flows within a $3d_b$ window at both sides from the boundaries of the compartments:

$$\phi_{c(i,j)} = A_{c(i,j)}\overline{u_{(i,j)}} \quad \text{where } \overline{u_{(i,j)}} = \sum_{k=1}^{N}(u_k d_{b,k}) \tag{2}$$

In Equation (2), $A_{c(i,j)}$ denotes the area of the interface between the adjacent compartments, u_k is the velocity at a particular sampling point at a $d_{b,k}$ distance from the intercompartmental boundary.

The turbulent intercompartment flows were determined using Equation (3). Similarly, as for the velocity, the turbulence kinetic energy was

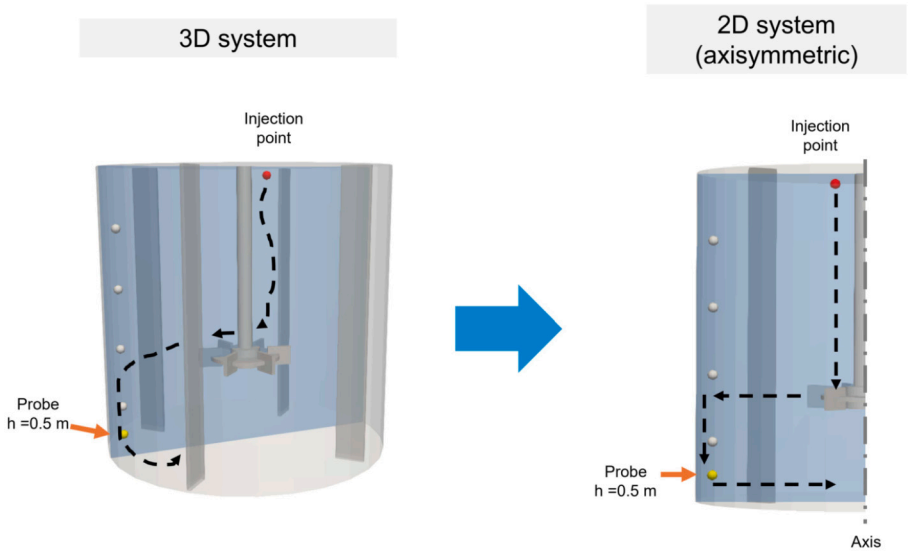


Fig. 4. Sketch of the system's simplification during a mixing experiment. The dotted line represents the streamline (L_s), following Groen (1994), for 3D and 2D-axisymmetrical representations to the farthest detection point. The light blue plane corresponds to the one used for extracting the data.

averaged using the relative distance to the boundary as a weighting factor. The overall exchange flows between compartments were calculated as introduced in Equation (1) and stored in a matrix **F**. Here the entries in each row describe the flows into compartment i from neighboring ones (Delafosse, 2014).

$$\phi_{t(i,j)} = A_{c(i,j)}\sqrt{2\overline{k_{t(i,j)}}/3} \text{ where } \overline{k_{t(i,j)}} = \sum_{p=1}^{N}(k_{tp}d_{b,k}) \tag{3}$$

It is important to note that some inaccuracies can be introduced during the sampling routine that might affect the predicted values for the intercompartmental flows and lead to mass imbalances over compartments. This is alleviated using a flow reconciliation routine that ensures mass conservation. This routine solves an optimization problem with equality constraints, which is defined as follows:

$$\hat{\mathbf{F}} = \underset{\mathbf{EF}=0}{\arg\min}(||\mathbf{F}_{meas} - \mathbf{F}||) \tag{4}$$

In Equation (4), $\hat{\mathbf{F}}$ is the reconciled flow matrix, $\mathbf{EF} = 0$ corresponds to the mass conservation constraint, where **E** is the coefficient matrix that contains entries of 1 for flows incoming and −1 for outgoing ones for each compartment, $\mathbf{F}_{meas}$ corresponds to the flow matrix as calculated from the data extracted from the CFD realizations. This problem is solved via a least-square routine embedded in the iterative `lsqr` method (The SciPy Community, 2024).

2.5. Dynamics through machine learning

To avoid having to run expensive CFD simulations for each new operating point, we use a machine learning module based on a feed-forward neural network developed in Tensorflow 2.16.2. This module infers the flow rates (ϕ_{rad} and ϕ_{ax}) upon changes in the filling level (H_L) and stirring speed (N_s) for fixed compartment layouts as outlined in the previous section. Hence, the smallest volume increments that can be resolved correspond to ≈2.95 m^3. This dynamic CM (dyn-CM) is based on Equation (5) such that a coarse representation of the system's hydrodynamics is obtained.

$$(\phi_{rad}, \phi_{ax}) = f(z_{pos}, r_{pos}, H_L, N_s) \tag{5}$$

The neural network had 13 hidden layers, after hyperparameter optimization using KerasTuner 1.4.7 (Further details can be found in Appendix C), each one containing 100 neurons. A learning rate of 2.290×10^{-3} was used during the training phase and 110 epochs. The Rectified Linear Unit (ReLU) function was used to drive neuron activation. The loss function of the neural network was based on the root mean square error (Equation (6)) between the observed ($\phi_{i,j}(\mathbf{x})_{obs}$) and predicted exchange flow rates ($\phi_{i,j}(\mathbf{x})_{pred}$).

$$MSE(w,b) = \frac{1}{2n}\sum_{\mathbf{x}}||\phi_{i,j}(\mathbf{x})_{obs} - \phi_{i,j}(\mathbf{x})_{pred}||^2 \tag{6}$$

In Equation (6), w are the weights gathered in the network, b is the biases, n is the number of inputs for training and **x** corresponds to the input vector containing the set of variables outlined in Equation (5). A set of CFD-CM parameterizations for stirred vessels with liquid volumes ranging from 63.5 to 123 m^3 and stirring rates from 0.25 to 1.46 s^{-1} were employed for training the neural network.

2.6. Validation

2.6.1. Mixing time determination

To assess the accuracy of the CM in replicating large-scale mixing, a comparison of the dimensionless 95% mixing time ($Nt_{m,95\%}$) from both CFD and CM realizations was made. Hence, the mixing time was determined using up to 5 probes, depending on the filling level, and considering a 95 % degree of homogeneity. The probes were placed at the radial position r = 2.25 m, axial positions h = 0.5, 1.0, 2.0, 4.0, and 6.0 m, and on the XY-plane rotated 45° along the vertical axis, such that the plane is between two baffles. The tracer was injected 0.25 m below the liquid surface, at a radial position r = 0.42 m at the opposite side of the probes (see Fig. 4). The CM results were validated against full CFD mixing simulations with equal operational settings; more details about the settings for the simulations used for determining the mixing time can be found in Appendix A.3.2.

For all the CM-based simulations, the dispersion of the tracer in the compartments corresponding to the coordinates of the probes mentioned above is tracked. In a similar way as outlined before, the mixing time is determined once the homogeneity degree of 95% is achieved.

2.6.2. Incorporating microbial kinetics

As a second means of evaluation, we compare substrate gradients which require a kinetic model. Thus, we incorporated the hyperbolic black-box kinetic model. The biomass-specific substrate uptake rate (q_s) is defined in Equation (7) as a function of the extracellular substrate con-

Table 1
Kinetic parameters for black-box model.

Parameter	Value	Unit
$q_{s,max}$	1.90×10^{-2}	$mol_s\ mol_x^{-1}\ h^{-1}$
α	1.00×10^{-3}	$mol_p\ mol_x^{-1}$
K_s	18.0×10^{-6}	$mol_s\ kg^{-1}$
$K_{s,I}$	2.50×10^{-6}	$mol_s\ kg^{-1}$
m_s	5.00×10^{-3}	$mol_s\ mol_x^{-1}\ h^{-1}$
$Y_{x/s}$	3.96	$mol_x\ mol_s^{-1}$
$Y_{x/s}$	0.174	$mol_p\ mol_s^{-1}$

Table 2
Initial conditions of the fermentation and molar mass of species involved.

Parameter	Value	Unit
$C_{s,0}$	150.0×10^{-6}	$mol_s\ kg^{-1}$
$C_{x,0}$	1.250	$mol_x\ kg^{-1}$
$V_{L,0}$	67.74	m^3
MW_s	180.2	$g_s\ mol_s^{-1}$
MW_x	28.05	$g_x\ mol_x^{-1}$

centration. Additionally, q_s is linked to growth, production, and maintenance via the Herbert-Pirt relation Equation (8). In this hypothetical example, we work with a black box kinetic model that was deliberately designed to be responsive to the effect of substrate gradients; Equation (9) gives a growth-coupled production term, that is inhibited at high extracellular substrate concentration. We stress this model is not based on any particular organism or product, it was chosen solely to demonstrate the potential impact of spatial heterogeneity in a fed-batch process, and allow comparison with an ideally mixed fed-batch model. These relations allow us to derive an expression for growth dependent on the substrate concentration (C_s).

$$q_s = q_{s,max}\left(\frac{C_s}{K_s + C_s}\right) \tag{7}$$

$$q_s = \frac{\mu}{Y_{x/s}} + \frac{q_p}{Y_{p/s}} + m_s \tag{8}$$

$$q_p = \alpha\mu\left(\frac{K_{s,I}}{K_{s,I} + C_s}\right) \tag{9}$$

In the previous equations, μ is the specific growth rate; m_s is the maintenance coefficient; K_s is the affinity constant to the substrate; $Y_{x/s}$ is the biomass to substrate yield; q_p is the specific product formation rate; $Y_{p/s}$ is the product to substrate yield; α is the proportionality constant of product formed; $K_{s,I}$ is the inhibition constant for product formation. The constant feeding rate of the substrate was set to $0.45\ mol_s\ s^{-1}$ at a 50 %(w/w) concentration. The density of the feed stream was assumed to be that of water at 25 °C. The values for the parameters of the metabolic model and initial conditions used in the present study can be found below in Tables 1 and 2, respectively.

3. Results and discussion

This section summarizes the results obtained from implementing the proposed workflow. First, a validation of the CFD-based compartment model (CFD-CM) is introduced by comparing the mixing time obtained via conventional CFD and CFD-CM realizations. This is followed by evaluating the accuracy of the inferring module to predict CM parameterizations upon changes in the working volume, referred to as the dynamic compartment model (dyn-CM). Later, the capabilities for predicting species transport and gradient evolution for a fed-batch operation are showcased. Finally, remarks on the current limitations and future developments of the dynamic CM approach are presented.

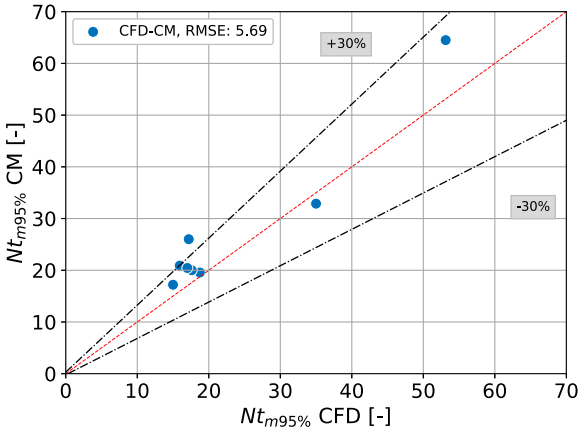


Fig. 5. Comparison of dimensionless mixing times calculated by the CFD-CM approach to CFD. Markers are simulations, the red dashed line is the parity line, and the black dashed lines represent the ±30 % error margin.

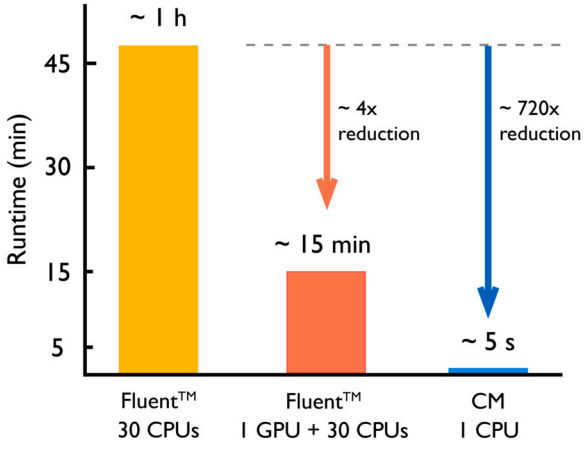


Fig. 6. Reduction in runtime corresponding only to a mixing experiment for realizations of a 98.2 m^3 stirred vessel using different methods. Note that time for resolving flow is not accounted for.

3.1. CFD-based compartment model (CFD-CM)

Fig. 5 compares the dimensionless mixing time (Nt) from the compartment model with those from the CFD simulations. These results suggest that the predictions from the compartmental layout allow for calculating the mixing times within a ±30 % error margin for CFD-based CM realizations. The extent of the error is attributed to the loss in resolution of the flow field and is similar to that reported in (Tajsoleiman et al., 2019). It was noted that the difference increases as the system deviates from the standard aspect ratio ($H/T > 1$) or has two stirrers.

Additionally, this comparison enabled the assessment of the capabilities of the low-resolution model for capturing the physical phenomena and the identification of trade-offs between the approaches regarding their predictive capabilities and the demand for computational resources. Hence, Fig. 6 shows that the CFD-CM approach outperformed the typical CFD workflow in terms of computational time for estimating the mixing time of a 98.2 m^3 vessel, even when leveraging GPU acceleration. Here, a reduction by up to a factor of ≈720 in runtime was obtained for estimating the mixing time when using a CPU-driven approach, where steady-state-like hydrodynamics is solved first and is followed by species transport using a frozen flowfield. Employing GPU acceleration for solving the flowfield resulted in a four-fold reduction when compared to the CPU-driven workflow.

A closer inspection of the coarser model was made by comparing the mixing curves and concentration maps of the system filled at several levels. The mixing curves were obtained from fully coupled CFD

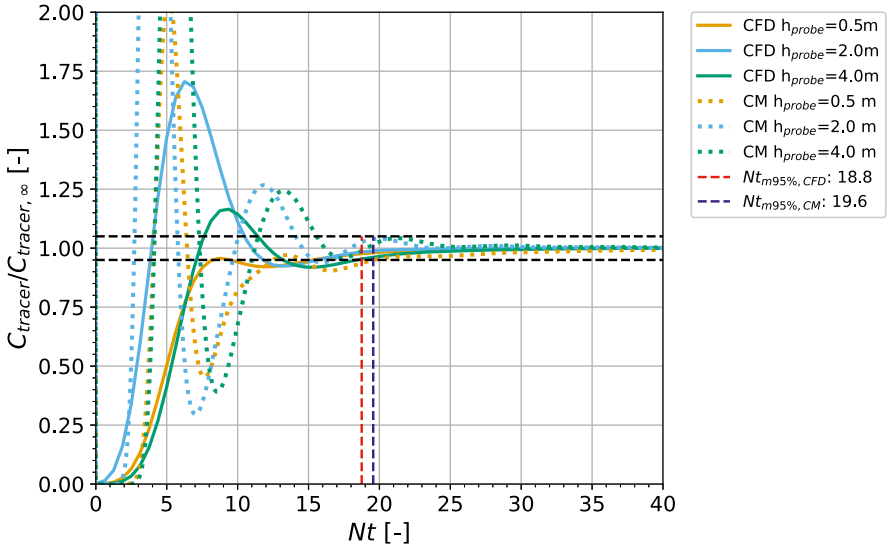


Fig. 7. Comparison of different response curves for determining the mixing time via the fully-coupled CFD and the CFD-CM model for a 98.2 m^3 tank.

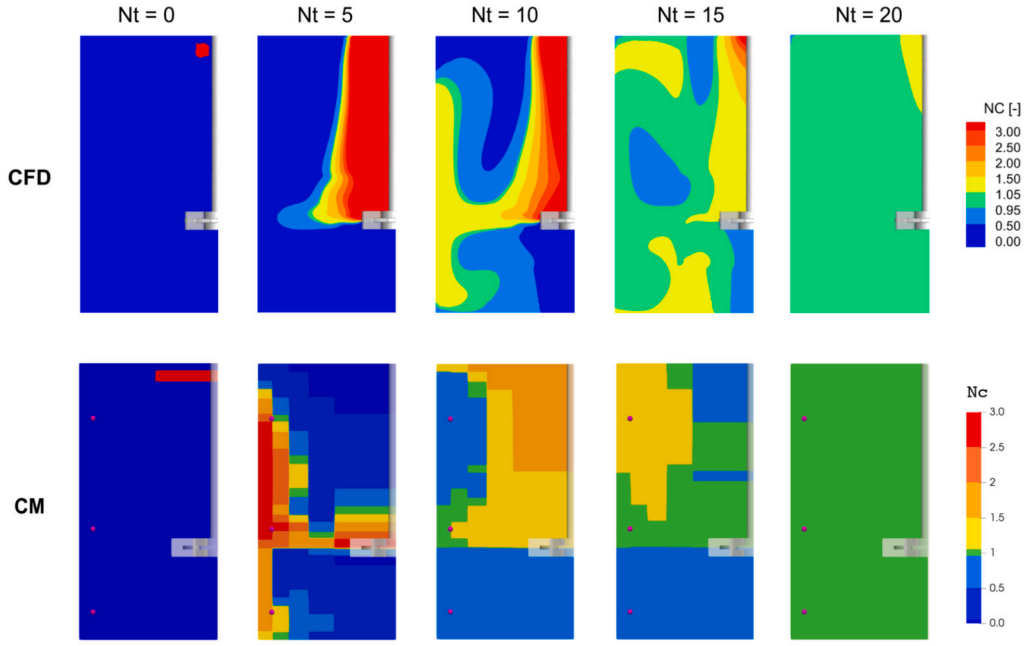


Fig. 8. Snapshots at different Nt values for a mixing experiment solved using a fully-coupled CFD simulation (top) and its CM counterpart (bottom) at an intermediate filling volume of 98.2 m^3. The plane shown corresponds to the one from Fig. 4.

and CFD-CM realizations. For example, Fig. 7 shows the curves for a filling volume of 98.2 m^3. Some deviations are observable between the response curves from the CFD and CFD-CM approaches that result in an 4.4 % underestimation of the dimensionless mixing time. It is important to note that the mixing time is determined by the response curve corresponding to the same probe location in both methods. In agreement with the mixing curves, the normalized concentration maps for the CFD-CM simulation (Fig. 8) show that this coarse realization predicts a faster local mixing but captures the patterns and overall mixing time predicted by CFD. The effect of this phenomenon on the prediction of fermentation profiles and gradients is addressed later.

These findings indicate that some phenomena are being lost given the settings and assumptions of the model (i.e., the axisymmetry of the system, selection of the plane from which the data are extracted, ideal mixing in the compartments, and ignoring the presence of the baffles). This abstraction of the CFD-CM approach suggests a localized faster dispersion of the tracer within the system, even though it delivers mixing times comparable with those obtained from CFD simulations. Such trends were also obtained for other realizations that can be consulted in Appendix B.3 and were previously reported and attributed to unresolved axial and radial flows (Delafosse, 2014; Haringa et al., 2022). Alleviating strategies might include incorporating a more rigorous evaluation based not only on the overall mixing phenomena (i.e., mixing time) but also on the lack of fit (i.e., RMSE) of the response curves as presented in (Cui et al., 1996), incorporating a constant for describing the intensity of mixing in the axial direction (Cui et al., 1996), using more recent compartmentalization approaches such as the ones outlined in (De Carfort et al., 2024; Haringa et al., 2022) or a combination thereof.

3.2. Dynamic compartment model (dyn-CM)

The previous section presented an analysis of the results obtained using exclusively a CFD-CM approach. However, these realizations are dependent on prior knowledge of the flow structure. Now we consider

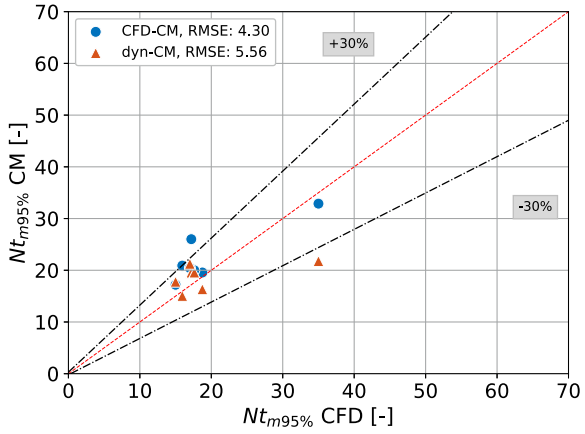


Fig. 9. Comparison of dimensionless mixing times calculated by CFD-CM and inferring module (dyn-CM). Markers are simulations, the red dashed line is the parity line, and the black dashed lines represent the ±30 % error margin.

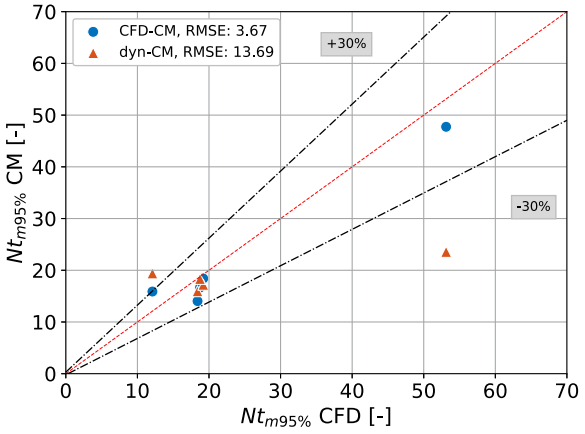


Fig. 10. Comparison of dimensionless mixing times calculated by the inferring module and CFD-CM for the testing points. Markers are simulations, the red dashed line is the parity line, and the black dashed lines represent the ±30 % error margin.

cases where the CM parameterization was predicted from a neural network. This was done to predict the exchange flow rates corresponding to intermediate filling volumes. Hence, this section focuses on assessing the inferring capabilities of the neural network-based parameterization, first, for conditions used during training and later, for unseen ones. This is followed by an inspection of the error in estimating the intercompartmental flow rates, presented as maps of local error.

3.2.1. Mixing inferred by the dyn-CM for training points

Fig. 9 shows the deviations for the dimensionless mixing times predicted by the CFD-CM and inferring module to the CFD and CFD-CM, respectively. Overall, the dyn-CM showed a good comparison with direct compartmentalization of the same CFD simulation, and adhered to the 30 % error compared with CFD which was observed for direct CM. Thus, highlighting the effect of the direct CFD-CM parameterization on the flow features and phenomena being captured (see Appendix B.1); hence, the results produced by the inference module. One exception was observed for a case where the system deviates from the standard aspect ratio (i.e., $H/T = 1.25$), the ML-based module provided a CM realization that estimated a mixing time out of the error margin deemed suitable for exploratory analysis. Similarly to the assessment of the CFD-CM approach, an analysis of the mixing curves revealed some differences from the ones obtained from fully coupled CFD simulations (see Appendix B.3). This is mainly attributed to the inherent simplifications introduced by the coarse-grained realizations via the CM approach rather than the estimations from the ML-based dynamic CM.

3.2.2. Mixing inferred for unseen operational conditions

Having established capabilities to replicate mixing times for training points, we move to testing points. The results for the unseen operating conditions used as a test set are shown in Fig. 10. The extreme points correspond to conditions out of the training space, for which the inferring module provided estimates with a relative error larger than ±30 %. For a fast mixing case (i.e., $V_L = 67.74\,\mathrm{m}^3$ and $N_s = 1.25\,\mathrm{s}^{-1}$) the mixing time was overpredicted by the dyn-CM by 60 % and for a slow mixing one (i.e., $V_L = 133\,\mathrm{m}^3$ and $N_s = 1.25\,\mathrm{s}^{-1}$), it was underpredicted by 56 %. This highlights that accuracy is significantly compromised when assessing conditions outside the training space. The evaluation of the intermediate cases corresponding to three intermediate filling volumes 67.74, 97.19, and 112.90 m^3 stirred at a rate of 1.25 s^{-1} revealed that the dyn-CM provides sufficiently accurate predictions for the mixing times of unseen working volumes. This comparison confirmed that the error of the mixing times reduces when using the dyn-CM as the working volume of the system increases. Analyzing the corresponding mixing curves revealed considerable limitations on the mixing behavior captured by the dyn-CM approach, especially for the 67.74 m^3 case. This is a consequence of the errors related to the estimations of the intercompartmental flow rates ($\phi_{(i,j)}$) at several locations of the corresponding compartment map, especially at the area where the axial flow from the impeller collides with the wall of the reactor. The assessment of such local errors for these three operating stages is presented in Appendix B.2. These current shortcomings can be mitigated by using more advanced compartmentalization approaches; we will explore refinement of the model for improved quantitative performance in follow-up work. For the current purposes of assessing the general approach, we deem the overall agreement is acceptable in representing the flow patterns, hence the mixing phenomena in the system at different operating points.

3.3. Tracking process dynamics through the proposed framework

The established framework for predicting flow patterns and mixing sets the stage for a more comprehensive analysis. Here, we evaluate its capabilities when coupling the workflow to a black-box kinetic model to estimate concentration profiles and gradient evolution. By integrating these concentration dynamics into our workflow, we can predict how species are dispersed throughout the reactor, providing deeper insights in the interplay between hydrodynamics, species transport, and microbial kinetics.

3.3.1. Fed-batch fermentation profiles

Fig. 11 shows the profiles of substrate and biomass during a 43-h long fed-batch fermentation obtained from an ideally-mixed model (IDM) and a dynamic compartment-based realizations updated on discrete volume increments ($\Delta V \approx 2.95\,\mathrm{m}^3$). This series of realizations required around 4.38 min to determine the spatiotemporal distribution of species, thus representing 1/500th of the fermentation duration.

For the biomass and product, discrepancies between the models were noticeable after 5 h of running the fermentation. This is mainly due to the inhibition of product formation in regions of the reactor where the substrate concentration is larger than $K_{s,I}$, thus diverting the substrate consumption towards growth. This is also reflected in the differences in the substrate profile obtained from both models. In the dyn-CM, slightly more substrate is present in the system but agrees with the trends predicted by the IDM. The reason for such deviations lies in the effect of both kinetics and transport encompassed in the first Damköhler number ($Da_I = \tau_{circ}/\tau_{rxn}$) where we take $\tau_{circ} \approx t_{m,95\%}/4$ and substrate consumption $\tau_{rxn} = K_s/(q_{s,max}C_x)$ (Haringa et al., 2018). Since $\tau_{rxn} \lesssim \tau_{circ}$, $Da_I \gtrsim 1$ after 10.5 h of fermentation, the occurrence of gradients was expected. This validates that the dynamic CM can capture the mixing phenomena with the added value of providing temporal and spatial information on species distribution. The 95% confidence interval of the

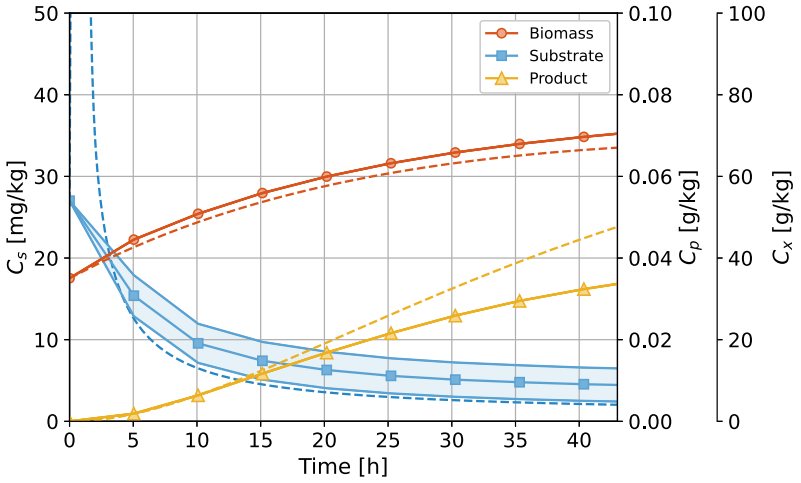
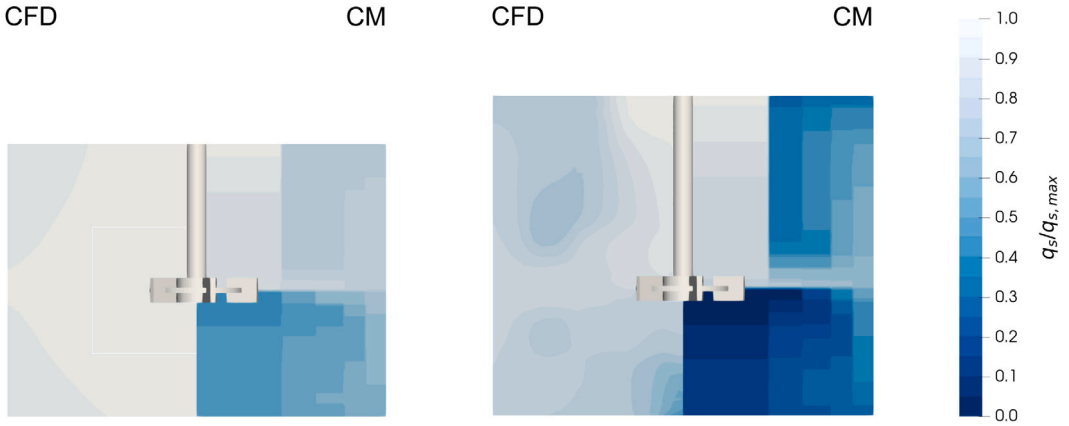


Fig. 11. Fed-batch fermentation profile for substrate (S), biomass (X), and product (P) using an ideally-mixed model (IDM) and a dynamic CM approach. Results from the IDM are shown as dashed lines, continuous lines with markers represent the volume-averaged concentrations from all the compartments of the dynamic CM simulations. Squares represent substrate, circles indicate biomass, and triangles denote product. The shaded region corresponds to the 95% confidence interval of the substrate concentration in the CM.



(a) 73.63 m^3 (b) 85.41 m^3

Fig. 12. Comparison of substrate uptake gradients ($q_s/q_{s,max}$) predicted by CFD (left) and dynamic CM (right) at different time points of the fed-batch fermentation. a) 10.0 h, and b) 30.5 h.

substrate concentration of the compartments shows the extent of the heterogeneity within the vessel, which is discussed in the following section.

3.3.2. Expected substrate consumption gradients

Estimation of the substrate consumption gradients was carried out assuming a homogeneous biomass concentration within the reactor. Hence, Fig. 12 shows the evolution of the substrate consumption gradients as $q_s/q_{s,max}$. The shape and extent of the major structures, such as the higher uptake rates closer to the feeding point and subsequent decrease in the bulk liquid, are captured by the dynamic CM approach and correspond to the ones predicted from CFD. Numerical differences occurred and were attributed to the reduction in overall spatial resolution and errors introduced by the parameterization of the CM as shown in Section 3.1, consequently being transferred to the dynamic CM approach. Such differences are evident for the regions below the impeller, where the dynamic CM predicts slower local mixing conditions than CFD; thus reducing the substrate availability.

In this particular case, the large value for the first Damköhler number ($Da_I > 1$) led to considerable gradients. The occurrence of these gradients resulted in the CM predicting 71.5 mol_p less than the IDM by the end of the fermentation (i.e., 30.3 %(w/w) decrease). This is because the ideal mixing model cannot locally capture the inhibition of the substrate in product formation, thus growth is under-predicted. This outcome confirms that the dynamic CM can capture the mixing phenomena while providing temporal and spatial information on species distribution. Furthermore, it reproduced to some extent the gradients observed in CFD at different time points despite the underlying assumptions.

The dynamic compartment model approach allows the prediction of the mixing phenomena as the liquid level rises. Thus, it enables the study of the evolution of the gradients as media is added to the system with a minute-long time expense; something infeasible with current CFD methods. For instance, such reduction might result in up to two orders of magnitude of runtime while using 1 CPU, which makes it amenable for design space exploration running several simulations in parallel in a computing cluster, rather than having to work sequentially as for CFD simulations. Hence, it constitutes a stepping stone for rapidly evaluating different designs, feeding strategies, and operating conditions. While this work focuses only on the formulation of the method and its implementation for a case study as proof of concept, it could equally be used for other fermentation processes.

3.4. Limitations and future developments

Our proposed method creates a dynamic, spatially resolved, and computationally efficient model. In this specific implementation for a

stirred tank bioreactor, it effectively captures the impact of liquid level variations and stirring speeds on mixing and gradient evolution with reasonable accuracy, while requiring minimal training data. This allows us to overcome one of the main limitations of compartment-based models for fed-batch processes by avoiding frequent recalibrations. However, some limitations remain and must be addressed. Three key areas to focus on in future developments include extending the capabilities to handle diverse geometrical and operational (e.g. airflow) features in the system, handling categorical variables for developing a more generic model with several reactor geometries, and improving the accuracy and easing the training of comparable ML-based methodologies.

Thus far, the introduced methodology does not account for different geometrical features such as several impellers or types of them, the number of baffles, cooling coils, other internals, or even different reactor geometries. Including such features will naturally require generating a new set of training data. Managing complex reactor geometries, such as airlifts with external circulation loops, will necessitate the implementation of an appropriate compartmentalization strategy, potentially similar to the one outlined in (De Carfort et al., 2024).

In its current formulation, the methodology is suitable for operating dynamic processes in a certain reactor design; such capabilities are similar to the ones provided by existing and emerging commercial platforms. The particular implementation in this work considers a single-phase case study. For aerated bioprocesses, further dynamics such as aeration (e.g., regime, bubble size, bubble coalescence, etc.) and changes in the physical properties of the medium (e.g. density, viscosity, and surface tension) are desired. To tackle this limitation, a suitable new CFD database simulating such dynamics is required, then it must be compartmentalized, and the dynamic CM must be retrained.

If a large CFD database is available, a generic model could be trained to cope with different geometries. Such a generic model would enable a broader industrial use of the proposed workflow. Nonetheless, dealing with categorical parameters would be required. Alternatives might include using transformers to update the existing model given new geometries without needing to retrain or using too much data. Moreover, increasing the number of operating conditions used as training data and refinement in the compartmentalization approach will lead to more accurate models, which will be explored in future studies.

Given the rapid advancements in machine learning, we can expect more accurate or easier-to-train methods for modeling dynamics to become available soon. Future work could explore alternative machine learning approaches, such as transformers (Alkin et al., 2024), convolutional neural networks, and physics-informed neural networks (Trávníková et al., 2024). These approaches have the potential to associate mechanical and operational features with engineering predictions based on CFD simulations. Thus, overcoming shortcomings of current approaches such as high data demand and physically inconsistent predictions/models. However, regardless of the specific architecture, the general approach remains the same: with enough CFD data, a learning model can effectively create dynamic reduced-order models for comprehensive process evaluation.

4. Conclusion

A software-agnostic method for creating a dynamic compartment model based on data extracted from CFD simulations for bioreactors was developed in this work. The model leverages the capabilities of compartment-based models and machine learning to infer model parameterizations for different filling volumes and stirring rates. This workflow proved useful for studying spatial and temporal heterogeneities in processes with varying working volumes like fed-batch fermentations.

The coarse compartmentalization layout estimated mixing times within a $\pm 30\,\%$ error margin compared to the ones predicted using high-resolution CFD, which agrees with previous studies. A similar error margin was observed in the dynamic compartment model, with greater deviations when inferring parameterizations out of the training space. However, the error was deemed reasonable for screening and preliminary analysis of fermentation operating conditions.

By coupling the workflow with a biokinetic model, the spatiotemporal calculation of species distribution during a 43 h long fed batch fermentation was resolved in 1/500th of the fermentation duration while accounting for varying working volumes. This provided insight not only into the fermentation profiles, which agree with the trends predicted by an ideal-mixed model but, also into the substrate stratification predicted by CFD at two time points. Thus, we demonstrate the ability of the model to provide insight into the so-called scale-up effects for fermentations.

The workflow we implemented can be further expanded to extend its current capabilities while preserving its essence: having sufficient CFD data available, a learning model is a promising means of creating dynamic reduced-order models for full-process evaluation. While we constrained ourselves to stirred tanks equipped with a single Rushton impeller for single-phase systems, evaluating other reactor configurations and designs must be plausible. Thus, this work aims to become a stepping stone for future works focused on implementing and refining the current workflow to enable the analysis of different and more complex geometries (e.g., impeller designs, combinations thereof, aspect ratios, etc.), multiphase systems (e.g., varying aeration rates), and cellular history via population balances or stochastic particle models using an approach based on the basic principle outlined in this work.

Nomenclature

Abbreviations

Abbreviation	Definition
A	Axial divisions
AMD	Advanced Micro Devices
CFD	Computational Fluid Dynamics
CRD	Computational Reaction Dynamics
CM	Compartment model
CV	Coefficient of variation
CPU	Central process unit
GPU	Graphics processing unit
IC	Intercompartmental
ML	Machine-learning
MRF	Multiple reference frame
R	Radial divisions
RAM	Random Access Memory
RT	Rushton Turbine
RTX	Ray Tracing Texel eXtreme

Symbols

Symbol	Definition	Unit
A_c	Cross-sectional area between compartments	m^2
b	Bias	-
C	Concentration	$mol\,kg^{-1}$
Da_I	First Damköhler number	-
d_b	Distance to boundary	m
e	Error	-
F	External forces	N
K	Constant	$mol\,kg^{-1}$
k_t	Turbulence kinetic energy	$m^2\,s^{-2}$
g	Gravity acceleration	$m\,s^{-2}$
H	Height	m
h	Axial position	m
M	Torque	$N\,m^{-1}$
m_s	Maintenance coefficient	$mol_s\,mol_x^{-1}\,h^{-1}$
N_{ax}	Number of axial divisions	-
N_c	Number of compartments	-
N_{rad}	Number of radial divisions	-
N_s	Stirring speed	s^{-1}
Nt	Dimensionless time	-

(*continued on next page*)

(*continued*)

Symbol	Definition	Unit
p	Pressure	$N\,m^{-2}$
q	Biomass specific rate	$mol\,mol_x^{-1}\,h^{-1}$
r	Radial position	m
T	Diameter of vessel	m
t	Time	s
u	Velocity component	$m\,s^{-1}$
V	Volume	m^3
w	Weights	-
Y	Molar yield	$mol\,mol^{-1}$
	Greek alphabet	
α	Product to biomass yield	$mol_p\,mol_x^{-1}$
ϵ	Specific power input	$W\,kg^{-1}$
ε	Turbulent energy dissipation rate	$m^2\,s^{-3}$
μ	Dynamic viscosity	$kg\,m^{-1}\,s^{-1}$
μ	Specific growth rate	h^{-1}
ρ	Density	$kg\,m^{-3}$
τ	Characteristic time	s
σ	Surface tension	$m\,s^{-1}$
ϕ	Intercompartmental flow rate	$m^3\,s^{-1}$
	Subscripts	
0	Ungassed conditions	
abs	Absolute	
ax	Axial	
C	Compartment	
c	Convective term	
circ	Circulation	
I	Inhibition	
i	Number of destination compartment	
j	Number of origin compartment	
k	Time step or element number	
L	Liquid	
m	Mixing	
meas	Measured	
p	Product	
pred	Predicted	
r	Radial	
rel	Relative	
rxn	Reaction	
s	Substrate	
t	Turbulent term	
x	Biomass	

CRediT authorship contribution statement

Héctor Maldonado de León: Writing – original draft, Software, Methodology, Formal analysis, Conceptualization. **Adrie Straathof:** Writing – review & editing, Supervision, Conceptualization. **Cees Haringa:** Writing – review & editing, Writing – original draft, Supervision, Software, Conceptualization.

Declaration of generative AI and AI-assisted technologies in the writing process

During the preparation of this work the author(s) ChatGPT 4.0 in order to improve language and readability. After using this tool/service, the author(s) reviewed and edited the content as needed and take(s) full responsibility for the content of the publication.

Declaration of competing interest

The authors declare that they have no known competing financial interests or personal relationships that could have appeared to influence the work reported in this paper.

Acknowledgements

This work was written as part of the Zero Emissions Biotechnology (ZEB) consortium at the Delft University of Technology. We would like to thank our colleagues in the TU Delft Bioprocess Engineering section for their input into valuable discussions.

Appendix A. CFD modeling

A.1. Reactor geometry

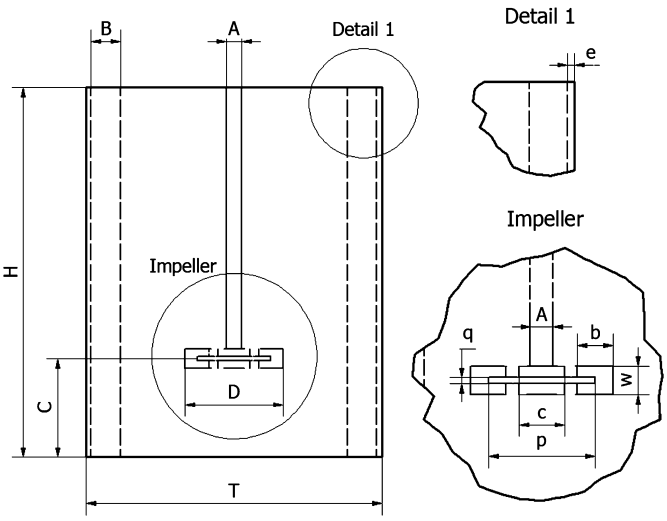


Fig. A.13. Sketch of the reactor geometry of up to 133 m^3. Details about the dimensions are presented in Table A.3.

Table A.3
Reactor dimensions for the different cases evaluated in this study.

Dimension	Value m	Description
T	5	Diameter of tank
H	3.22 up to 6.77	Height of tank
D	1.67	Diameter of impeller
A	0.27	Shaft diameter
B	0.50	Width of baffle
C	1.67	Bottom clearance of impeller
e	0.085	Clearance between baffles and walls
b	0.417	Width of impeller blade
w	0.334	Height of impeller blade
c	0.533	Diameter of impeller coupling to shaft
q	0.067	Thickness of impeller disk
p	1.25	Diameter of impeller disk

A.2. Meshing

After placing all the elements required for each reactor configuration in an `assembly` file in *Autodesk® Inventor Professional™ 2021*, the generated geometry was exported as `.step` file, that was imported in *Ansys SpaceClaim 2023 R1™* for checking for any for defects, extra edges, and missing faces. Then, a `.pmdb` file containing the geometry and the definition of the boundary conditions was created. This file was imported in *Ansys Fluent Meshing™* for creating the geometry mesh for each case of study. Since the aim of this work focuses on the fluid domain within the reactor, the impellers and baffles were extracted from the reactor geometry. Details about the meshing workflow can be found in Tables A.4 and A.5, any parameter that is not described should be taken as the default one.

A.3. CFD setup

In this section, we describe the settings and models that were implemented for the different simulations regarding this work. The following models are treated: turbulence and species transport along with their respective parameters.

Table A.4
Typical parameters when meshing the different reactor geometries.

Meshing parameter	Value/option
Workflow	Watertight meshing workflow
Local sizing	
Growth rate	1.2
Size control type	Body_Size
Target mesh size [m]	0.025
Surface mesh	
Minimum size [m]	0.025
Maximum size [m]	0.2
Growth rate	1.2
Describe geometry	
Type	Only fluid with no voids
Change from wall to internal	Yes
Share Topology	No
Local Boundary Layers	
Walls	
Offset method type	smooth-transition
Number of layers	3
Transition ratio	0.272
Growth rate	1.2
Add in	fluid-regions
Grow on	Tank_walls
Transition rotorbox	
Offset method type	smooth-transition
Number of layers	3
Transition ratio	0.25
Growth rate	1.15
Add in	fluid-regions
Grow on	Rotorbox_walls

Table A.5
Typical parameters when meshing the different reactor geometries - cont.

Meshing parameter	Value/option
Volume mesh	
Fill with	poly-hexcore
Buffer layers	2
Peel layers	2
Min cell length [m]	0.025
Max cell length [m]	0.2
Improve volume mesh	
Improve cell quality limit	0.3

A.3.1. Turbulence model

Due to known experimental observations for the flow behavior in stirred tank reactors, along with proven comparisons of simulations, the *Standard* $k-\varepsilon$ model was implemented in *Ansys Fluent*™ by setting the `viscous` model with the parameters listed in Table A.6.

Table A.6
Parameters for the viscous model accounting for turbulence.

Viscous model	
Model	k-epsilon
k-epsilon model	Standard
Near-wall treatment	Standard wall functions
Model constants	
Cmu	0.09
C1-epsilon	1.44
C2-epsilon	1.92
TKE Parndtl Number	1.00
TDR Prandtl Number	1.3
Energy Prandtl Number	0.85
Wall Prandtl Number	0.85

Table A.7
Parameters for injection point of inert tracer in the STR models.

Parameter	Value
Name	Tracer inlet
Shape	Sphere
Coordinates [m]	
x-center	-0.30
y-center	0.25 offset from surface
z-center	0.30
Radius [m]	0.075

Table A.8
Parameters for the `species` model when running the mixing time tests.

Species model		
Model	Species transport	-
Phase properties		
Phase	Liquid	-
Phase material	water-tracer	-
Water-tracer mixture properties		
Compounds in mixture	1. tracer	-
	2. water	-
Density	Volume weighted-mixing-law	$kg\,m^{-3}$
Viscosity	1.00×10^{-3}	$kg\,m^{-1}\,s^{-1}$
Mass diffusivity	dilute-approx	-
Diffusion coefficient for tracer	1.00×10^{-9}	$m^2\,s^{-1}$

A.3.2. Species transport

The mixing time determination was done by simulating the injection of an inert tracer within the liquid domain and assuming a batch vessel. In *Ansys Fluent*™ this transient simulation ($\Delta t = 0.01$ s) is performed by patching a zone that corresponds to the point of injection with the settings outlined in Table A.7. The molar concentration was set to 1.0 $kmol\,m^{-3}$. Additionally, a set of measuring points was defined to record the molar tracer's concentration at different locations along a 45-degree-rotated XY-plane (see Fig. 4). For all the tests where a tracer injection was needed, the properties and parameters shown in Table A.8 were defined for the species model.

As shown in Table A.8, a mixture called `water-tracer` was created. This consists of the `water` and a copy of it. However, some properties had to be changed from the default mixture template as shown in the corresponding section of Table A.8.

A.3.3. Discretization schemes

Table A.9 shows the PV-coupling and spatial discretization schemes implemented in all the evaluated fully-coupled CFD models. Also, the specifications for the solution controls are shown. If not mentioned, the value for a specific option must be taken as the default one for Ansys FLUENT 2023R1.

A.3.4. Under-relaxation factors

In addition, a set of under-relaxation factors (URFs) were modified. This was done since a `pressure-based` coupled algorithm was selected for solving the model with the non-linear nature of the equations being solved. The factors implemented can be consulted in Table A.9.

A.4. Operating conditions for simulations generated to train and validate the workflow

Table A.10 details the simulations used for training and testing the inferring module developed in this work. Also, the results for the dimensionless mixing times obtained from CFD, CFD-CM, and dyn-CM are provided.

Table A.9
Discretization schemes used for the solution of transient simulations for the evaluated single-phase setups in this work.

Solution methods		Solution controls
Pressure-velocity coupling		
Scheme	SIMPLE	
Spatial discretization		
Gradient	Least squares Cell Based	
Pressure	Second Order	0.3
Density	Second order upwind	0.5
Momentum	Second order upwind	0.45
Turbulent kinetic energy	Second order upwind	0.4
Specific dissipation rate	Second order upwind	0.4
Tracer[a]	Second order upwind	0.99
Transient formulation[a]	Second order implicit	-

[a] Used only when solving for the mixing-time analyses.

Table A.10
Operating parameters and dimensionless mixing times for simulations employed in this study.

Set	Working volume V_L/(m^3)	Stirring speed N_s / (s^{-1})	CFD Nt / (−)	CFD-CM Nt / (−)	dyn-CM Nt / (−)
Training	98.2	1.4	24	22.3	22.7
Training	98.2	0.040	20	23.0	33.4
Training	98.2	1.5	17	26.0	19.5
Training	98.2	0.75	16	20.9	15.1
Training	98.2	1.3	19	19.6	16.3
Training	73.6	0.25	18	20.0	19.6
Training	73.6	1.3	17	20.4	21.3
Training	63.5	1.3	15	17.2	17.8
Training	123	1.3	35	32.9	21.8
Test	133	1.3	53	47.7	23.6
Test	97.2	1.3	18	14.0	16.0
Test	73.6	1.3	17	14.6	21.3
Test	113	1.3	19	18.4	17.2
Test	67.7	1.3	12	15.9	19.4

Appendix B. Compartment modeling

B.1. Effect of compartmentalization layout on predicting capabilities

Different combinations of divisions on the three axes were used to establish the most suitable compartmentalization layout for this study. Fig. B.14 shows the effect of several layouts on the dimensionless mixing times predicted by the compartment model. The shaded band in Fig. B.14 represents the error deemed suitable for design space exploration when conducting scale-up studies. Prior studies have suggested that the layout should match naturally occurring boundaries in the flow-field such that flow patterns are preserved (Cui et al., 1996; Haringa et al., 2022; Vrábel et al., 2000). Such boundaries are the midplane between impellers and the unidirectional discharge flow of radial impellers. These boundaries result from colliding circulation loops established in the axial direction (Groen, 1994). Hence, the most suitable layout to preserve the flow patterns, provide sound estimates of mixing times, and match many of the liquid heights in the training set was the one with 5 radial divisions, and as many axial ones with a separation of 15 cm that approximated the boundary of the circulation loops at the impeller discharge.

B.2. Local error maps

Any inaccuracy in estimating the exchange flow rates between compartments drives the deviations from the ground truth (i.e., CFD simulations). Here we focus on three intermediate filling volumes: 67.74, 97.19, and 112.90 m^3. Fig. B.15 shows a comparison of the mixing time predicted by the different methods employed in this work.

To assess the accuracy of the intercompartmental flow rate estimations from the dyn-CM approach, the absolute and relative error in each compartment were calculated Equations (B.1) and (B.2). Hence, Figs. B.16 and B.17 show the relative and absolute error maps of the velocity magnitude, respectively, for the realizations using the dyn-CM approach for the operating states of 67.74, 97.19, and 112.90 m^3 at a stirring rate of 1.25 s^{-1}.

$$e_{\phi,abs} = |\phi_{(ij),dyn-CM}| - |\phi_{(ij),CM}| \tag{B.1}$$

$$e_{\phi,rel} = \frac{|\phi_{(ij),dyn-CM}| - |\phi_{(ij),CM}|}{|\phi_{(ij),CM}|} * 100\% \tag{B.2}$$

The local error maps suggest that the predictive module (i.e., dyn-CM-based model) fails to accurately estimate the velocity components for some compartments where high velocities (e.g., closer to the impeller zone, sudden changes in the direction of the flows) or stagnant zones are expected (e.g., the bottom wall of the reactor, free surface, and center of axial circulation loops). These regions are characterized by the dominance of flows in a particular direction, thus a zero flow rate in another. For example, the flow rates for the compartments close to the wall of the reactor are predominantly axial, thus any radial component lacks physical relevance. This results in a compartment for which the relative error is larger than 100 % (see Fig. B.16c) but the abso-

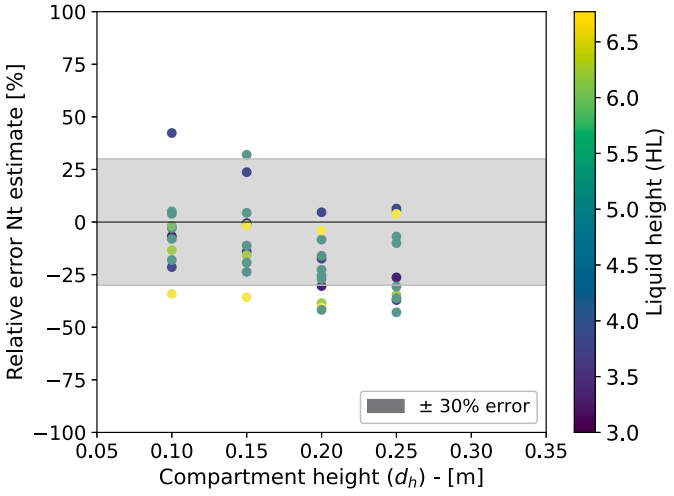


Fig. B.14. Comparison of different compartment heights (d_h) for creating the 2D compartmentalization layout of several realizations of the stirred tank system (i.e., varying H_L).

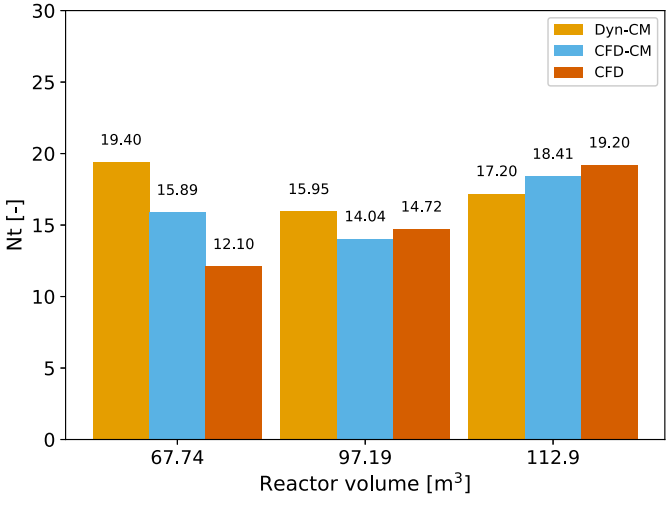
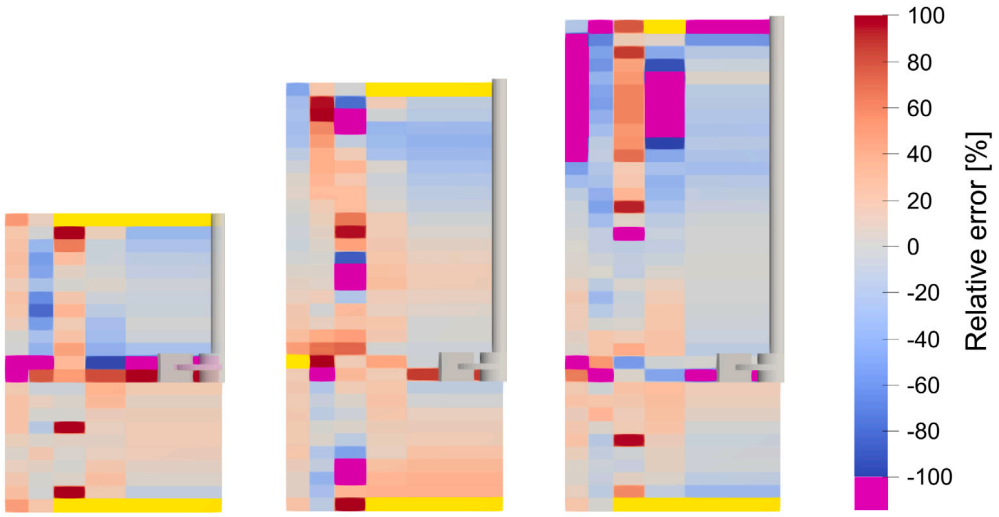
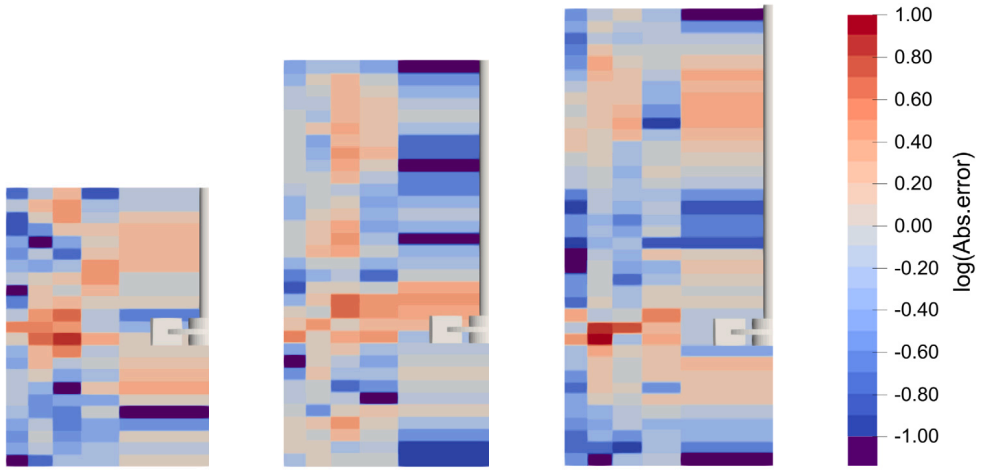


Fig. B.15. Comparison of mixing times calculated via the Dyn-CM, CFD-CM, and fully-coupled CFD simulations for the intermediate filling volume of 67.74, 97.19, and 112.9 m^3, respectively.



(a) 67.74 m^3 (b) 97.19 m^3 (c) 112.90 m^3

Fig. B.16. Relative error maps for realizations obtained from the dyn-CM approach for different working volumes. Magenta regions correspond to out-of-range error values; the bright yellow ones result in a numerical overflow.



(a) 67.74 m^3 (b) 97.19 m^3 (c) 112.90 m^3

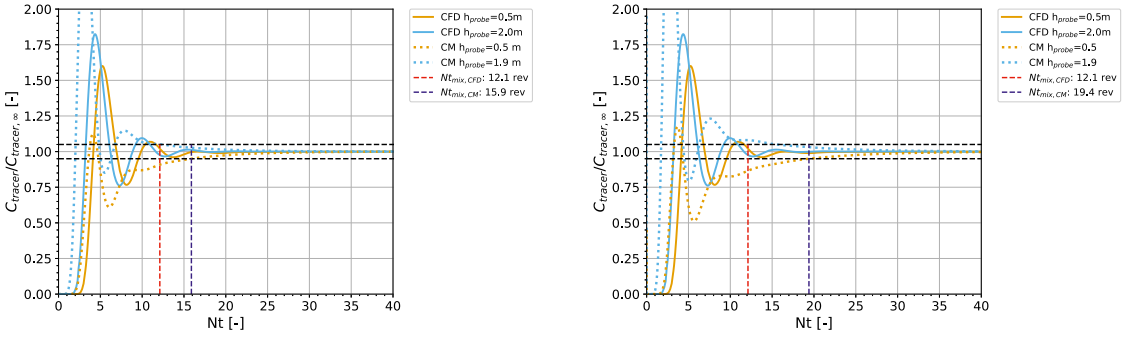
Fig. B.17. Absolute error maps for realizations obtained from the dyn-CM approach for different working volumes. To ease the visualization, the data is presented in logarithmic values; where the purple regions correspond to below-range values.

lute error does not exceed 10 $m\,s^{-1}$ (see Fig. B.17c). For the case of the top surface and bottom wall, the error results in a numerical overflow since the axial component should not be present. Yet, this component is assigned a value different from zero (see Figs. B.16a to B.16c). These spurious predictions are mostly remediated during the flow reconciliation step. A closer inspection revealed that initial estimates might result in a six-fold deviation and, later, be reduced to 0.25 times the actual value. Nevertheless, further mitigation strategies are deemed necessary to avoid complete reliance on the reconciliation flow that solely closes the mass balance without any extra source of information about the direction of the flows other than the estimate provided by the model based on the neural network. In this regard, implementing a hybrid loss function that combines a data-driven term and a physics-based one that ensures mass conservation might be a sensible alternative.

Despite large local errors, we conclude the overall agreement is acceptable to represent the flow patterns, hence the mixing phenomena in the system at different operating points. We showcase its capabilities to provide means for the spatiotemporal analysis of the species distribution in a fed-batch fermentation process.

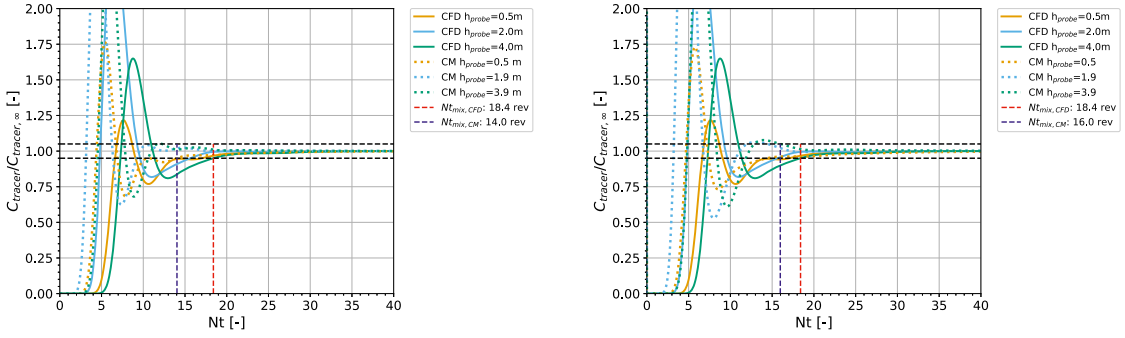
B.3. Comparison of preserved mixing phenomena using the CFD-CM, and dyn-CM approaches to CFD

Several realizations for different reactor filling volume conditions were generated using the CFD-CM approach presented in this work. These simulations allow an understanding of the effects of simplifying the system on the response curves of the mixing phenomena (see Figs. B.18 to B.22). Simplifications correspond to assuming axisymmetry, thus considering the mixing as occurring only in the axial direction and discretizing the system using ideally mixed volumes. These simplifications resulted in an abrupt increase in the normalized concentration of the tracer compared to the one predicted by CFD simulations, even when the peak-detection and plateau-reaching times are comparable to each other. Thus, it confirms that the CFD-CM approach, while achieving the system's homogeneity at similar times to CFD and from the same limiting probe, reduces the resolution of the phenomena within the system. This could be alleviated by introducing the third dimension in cartesian or polar coordinates (i.e., tangential direction) as previously introduced in (De Carfort et al., 2024) and (Haringa et al., 2022), respectively.



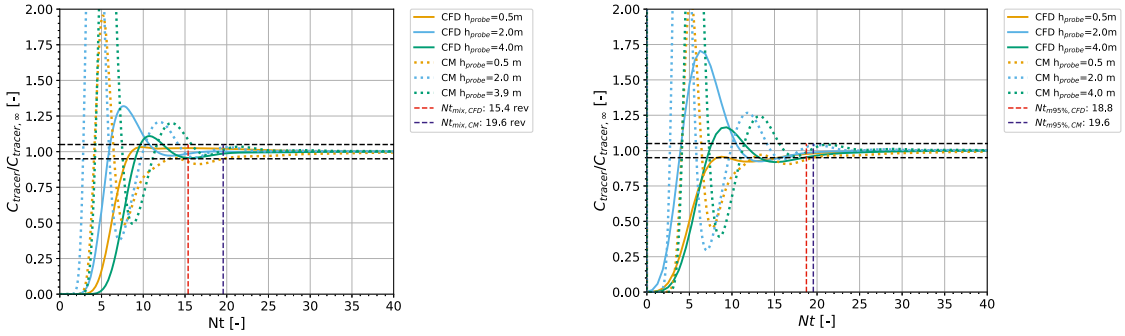
(a) CFD-CM (b) dyn-CM

Fig. B.18. Comparison of mixing curves from CFD-CM or dyn-CM (dotted) to CFD (solid) realizations at 67.74 m^3.



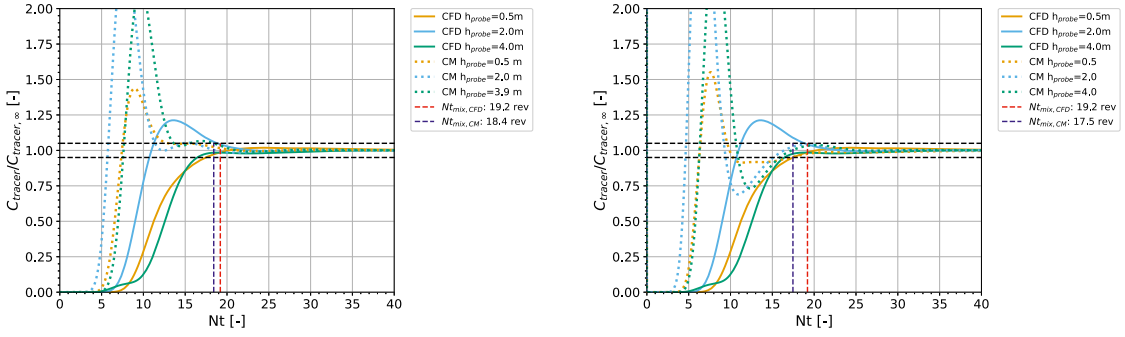
(a) CFD-CM (b) dyn-CM

Fig. B.19. Comparison of mixing curves from CFD-CM or dyn-CM (dotted) to CFD (solid) realizations at 97.20 m^3.



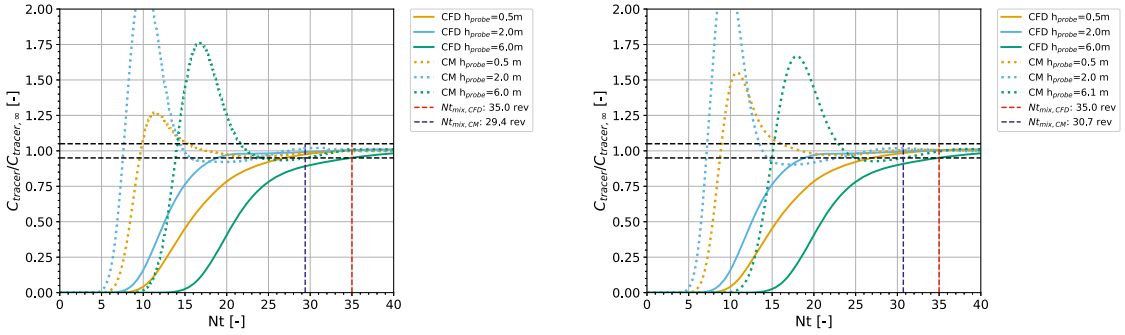
(a) CFD-CM (b) dyn-CM

Fig. B.20. Comparison of mixing curves from CFD-CM or dyn-CM (dotted) to CFD (solid) realizations at 98.20 m^3.



(a) CFD-CM (b) dyn-CM

Fig. B.21. Comparison of mixing curves from CFD-CM or dyn-CM (dotted) to CFD (solid) realizations at 112.9 m^3.



(a) CFD-CM (b) dyn-CM

Fig. B.22. Comparison of mixing curves from CFD-CM or dyn-CM (dotted) to CFD (solid) at 122.7 m^3.

Table C.11
Configuration of the best three models after hyperparameter optimization.

Trial	Layers	Learning rate	Validation loss
690	13	1.814×10^{-3}	2.28971×10^{-3}
249	16	0.687×10^{-3}	2.41021×10^{-3}
332	18	0.705×10^{-3}	2.55433×10^{-3}

Some greater deviations from CFD for predicting the mixing times when using the dyn-CM approach were observed. Similarly as for the CFD-CM approach, mixing curves were generated for seen and unseen operating stages, which revealed some spurious predictions for the exchange flow rates resulting in a loss of accuracy in predicting the mixing times. However, that loss of accuracy did not result in a loss of the overall phenomena being predicted by the dyn-CM approach.

Appendix C. Hyperparameter optimization

A hyperparameter optimization was performed using the `keras tuner` package over 1000 trials to find a more efficient inference model. The `RandomSearch` method was used for the tuner, and during the training, an `EarlyStopping` callback was used with a patience parameter of 20. After these, it was found that the topology with 13 hidden layers comprised of 100 neurons each and using a learning rate of around 1.814×10^{-3} provided the best validation loss of around 2.290×10^{-3} after 110 to 160 iterations. The optimization routine provided three other candidates with different topologies and hyperparameters that are summarized in Table C.11. The corresponding plots for the training and validation losses are shown in Fig. C.23, and the corresponding models are provided in the repository along with the data used for training.

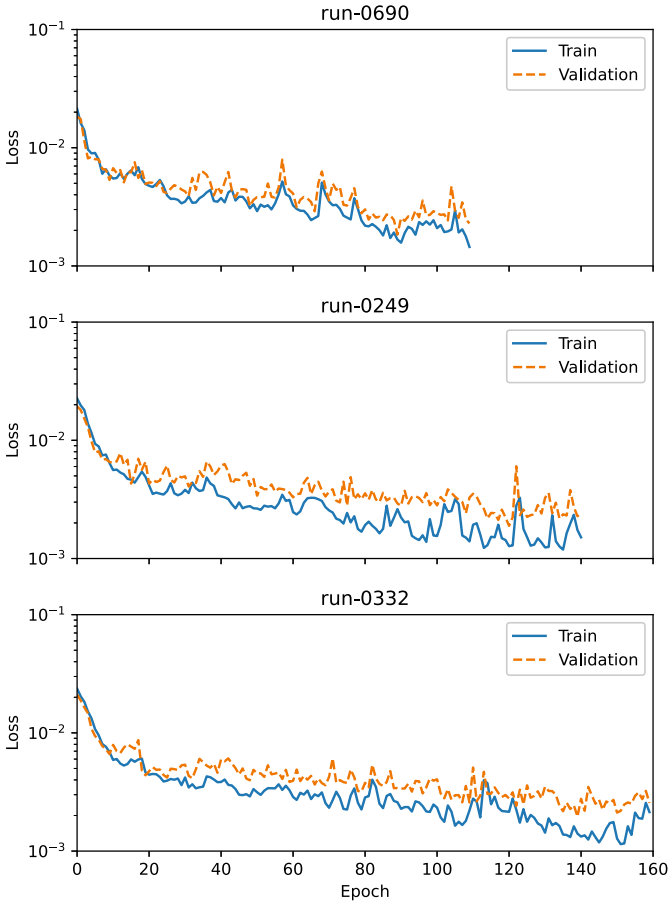


Fig. C.23. Loss plots for the best three configurations during hyperparameter optimization.

Data availability

All relevant data generated or analyzed during this study is available at the 4TU.Data Repository (DOI: https://doi.org/10.4121/0a08d2ec-8959-403f-afea-2b085dc9f3a6).

References

Alkin, B., Fürst, A., Schmid, S., Gruber, L., Holzleitner, M., Brandstetter, J., 2024. Universal physics transformers: a framework for efficiently scaling neural operators. https://arxiv.org/abs/2402.12365. arXiv:2402.12365, 2024.

Bai, Y., Fonte, C.P., Kowalski, A., Rosales-Trujillo, W., Rodgers, T.L., 2023. A general methodology for extracting and categorising flow patterns in turbulent stirred tank mixers based on 2-d network-of-zones (noz) model. Chem. Eng. Res. Des., 829–841. https://doi.org/10.1016/j.cherd.2023.05.022.

Bylund, F., Collet, E., Enfors, S.-O., Larsson, G., 1998. Substrate gradient formation in the large-scale bioreactor lowers cell yield and increases by-product formation. Bioprocess Eng. 18, 171. https://doi.org/10.1007/s004490050427.

Couper, J., Penney, R., Fair, J., Walas, S., 2012. Mixing and agitation. In: Chemical Process Equipment - Selection and Design. Elsevier, pp. 277–327.

Crater, J.S., Lievense, J.C., 2018. Scale-up of industrial microbial processes. FEMS Microbiol. Lett. 365, fny138. https://doi.org/10.1093/femsle/fny138.

Cui, Y., van der Lans, R., Noorman, H., Luyben, K., 1996. Compartment mixing model for stirred reactors with multiple impellers. Trans. Inst. Chem. Eng. 74, 261–271.

De Carfort, J.L., Pinto, T., Krühne, U., 2024. An automatic method for generation of CFD-based 3D compartment models: towards real-time mixing simulations. Bioengineering 11, 169. https://doi.org/10.3390/bioengineering11020169.

Delafosse, A., 2014. CFD-based compartment model for description of mixing in bioreactors. Chem. Eng. Sci. 106, 76–85.

Delvigne, F., Takors, R., Mudde, R., van Gulik, W., Noorman, H., 2017. Bioprocess scale-up/down as integrative enabling technology: from fluid mechanics to systems biology and beyond. Microb. Biotechnol. 10, 1267–1274. https://doi.org/10.1111/1751-7915.12803.

Groen, D., 1994. Macromixing in Bioreactors. Ph.D. thesis. Delft University of Technology. https://resolver.tudelft.nl/uuid:3ac019f1-d19a-4853-9a29-554f1149bd5b.

Haringa, C., Mudde, R.F., Noorman, H.J., 2018. From industrial fermentor to CFD-guided downscaling: what have we learned? Biochem. Eng. J. 140, 57–71. https://doi.org/10.1016/j.bej.2018.09.001.

Haringa, C., Tang, W., Noorman, H.J., 2022. Stochastic parcel tracking in an Euler–Lagrange compartment model for fast simulation of fermentation processes. Biotechnol. Bioeng. 119, 1849–1860. https://doi.org/10.1002/bit.28094.

Herwig, C., Pörtner, R., Möller, J. (Eds.), 2021. Digital Twins: Applications to the Design and Optimization of Bioprocesses. Advances in Biochemical Engineering/Biotechnology, vol. 177. Springer International Publishing, Cham.

Jourdan, N., Neveux, T., Potier, O., Kanniche, M., Wicks, J., Nopens, I., Rehman, U., Le Moullec, Y., 2019. Compartmental modelling in chemical engineering: a critical review. Chem. Eng. Sci. 210, 115196. https://doi.org/10.1016/j.ces.2019.115196.

Kampers, L.F., Asin-Garcia, E., Schaap, P.J., Wagemakers, A., Martins dos Santos, V.A., 2022. Navigating the valley of death: perceptions of industry and academia on production platforms and opportunities in biotechnology. EFB Bioeconomy Journal 2, 100033. https://doi.org/10.1016/j.bioeco.2022.100033.

Lapin Alexei, M.D., Reuss, M., 2004. Dynamic behavior of microbial populations in stirred bioreactors simulated with Euler-Lagrange methods: traveling along the lifelines of single cells. Ind. Eng. Chem. Res., 4647–4656.

Lapin Alexei, S.J., Reuss, M., 2006. Modelling the dynamics of e.coli populations in the three-dimensional turbulent field of a stirred-tank bioreactor - a structured -segregated approach. Chem. Eng. Sci., 4783–4797.

Lara, A., Galindo, E., Ramírez, O., Palomares, L., 2006. Living with heterogeneities in bioreactors: understanding the effects of environmental gradients on cells. Mol. Biotechnol. 34, 355–381. https://doi.org/10.1385/MB:34:3:355.

Losoi, P., Konttinen, J., Santala, V., 2022. Substantial gradient mitigation in simulated large-scale bioreactors by optimally placed multiple feed points. Biotechnol. Bioeng. 119, 3549–3566. https://doi.org/10.1002/bit.28232.

Nadal-Rey, G., McClure, D.D., Kavanagh, J.M., Cassells, B., Cornelissen, S., Fletcher, D.F., Gernaey, K.V., 2021a. Development of dynamic compartment models for industrial aerobic fed-batch fermentation processes. Chem. Eng. J. 420, 130402. https://doi.org/10.1016/j.cej.2021.130402.

Nadal-Rey, G., McClure, D.D., Kavanagh, J.M., Cornelissen, S., Fletcher, D.F., Gernaey, K.V., 2021b. Understanding gradients in industrial bioreactors. Biotechnol. Adv. 46, 107660. https://doi.org/10.1016/j.biotechadv.2020.107660. https://www.sciencedirect.com/science/article/pii/S0734975020301622.

Neubauer, P., Junne, S., 2010. Scale-down simulators for metabolic analysis of large-scale bioprocesses. Curr. Opin. Biotechnol. 1, 114–121. https://doi.org/10.1016/j.copbio.2010.02.001.

Noorman, H., 2011. An industrial perspective on bioreactor scale-down: what we can learn from combined large-scale bioprocess and model fluid studies. Biotechnol. J. 6, 934–943. https://doi.org/10.1002/biot.201000406.

Oliveira, C.L., Pace, Z., Thomas, J.A., DeVincentis, B., Sirasitthichoke, C., Egan, S., Lee, J., 2024. Cfd-based bioreactor model with proportional–integral–derivative controller functionality for dissolved oxygen and ph. Biotechnol. Bioeng. 121, 655–669. https://doi.org/10.1002/bit.28598.

Puiman, L., Abrahamson, B., Lans, R.G.V.D., Haringa, C., Noorman, H.J., Picioreanu, C., 2022. Alleviating mass transfer limitations in industrial external-loop syngas-to-ethanol fermentation. Chem. Eng. Sci. 259, 117770. https://doi.org/10.1016/j.ces.2022.117770.

Siebler, F., Lapin, A., Hermann, M., Takors, R., 2019. The impact of co gradients on C. Ljungdahlii in a 125 m^3 bubble column: mass transfer, circulation time and lifeline analysis. Chem. Eng. Sci. 207, 410–423.

Tajsoleiman, T., Spann, R., Bach, C., Gernaey, K.V., Huusom, J.K., Krühne, U., 2019. A CFD based automatic method for compartment model development. Comput. Chem. Eng. 123, 236–245. https://doi.org/10.1016/j.compchemeng.2018.12.015.

The SciPy Community, 2024. lsqr.

Trávníková, V., Wolff, D., Dirkes, N., Elgeti, S., von Lieres, E., Behr, M., 2024. A model hierarchy for predicting the flow in stirred tanks with physics-informed neural networks. Advances in Computational Science and Engineering 2, 91–129. https://doi.org/10.3934/acse.2024007.

Vrábel, P., van der Lans, R., Luyben, K., Boon, L., Nienow, A., 2000. Mixing in large-scale vessels stirred with multiple radial or radial and axial up-pumping impellers: modelling and measurements. Chem. Eng. Sci. 55, 5881–5896. https://doi.org/10.1016/S0009-2509(00)00175-5.

Xu, B., Jahic, M., Blomsten, G., Enfors, S., 1999. Glucose overflow metabolism and mixed-acid fermentation in aerobic large-scale fed-batch processes with escherichia coli. Applied Microbial Biotechnology, 564–571.